ACS Partner Journal

CHEM & BIO ENGINEERING

pubs.acs.org/ChemBioEng

Article

Hollow Bismuth-Based Nanoreactor with Ultrathin Disordered Mesoporous Silica Shell for Superior Radioactive Iodine Decontamination

Zhenjiang Tian, Tien-Shee Chee, Yuxun Hao, Kang Kang, Xiaofan Yang, and Chengliang Xiao*

Cite This: *Chem Bio Eng.* 2024, 1, 548−558

Read Online

ACCESS | Metrics & More | Article Recommendations | Supporting Information

ABSTRACT: The effective removal of radioactive iodine under harsh high-temperature conditions, akin to those encountered in real spent nuclear fuel reprocessing, remains a formidable challenge. Herein, a novel bismuth-based mesoporous silica nanoreactor with a distinctive hollow yolk−shell structure was successfully synthesized by using silica-coated Bi_2O_3 as a hard template and alkaline organic ammonia for etching (Bi@HMS-1, HMS = hollow mesoporous silica). In contrast to conventional inorganic alkali-assisted methods with organic template agents, our approach yielded a material with thinner and more disordered shell layers, along with a relatively smaller pore volume. This led to a significant reduction in the physisorption of Bi@HMS-1 onto iodine while maintaining a smooth passage of guest iodine molecules into and out of the shell channels. Consequently, the resulting sorbent exhibited an outstanding iodine sorption capacity at high temperatures, achieving a chemisorption percentage as high as 96.5%, which makes it extremely competitive among the currently reported sorbents.

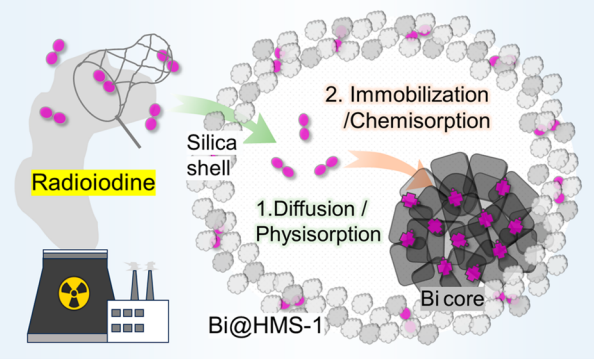

KEYWORDS: *Bismuth, I_2, Capture, Core−shell, Mesoporous silica*

INTRODUCTION

While nuclear reactors play a crucial role in supplying society with clean energy, the inevitable byproduct is the generation of a substantial amount of radioactive waste.[1,2,54] Among these waste products, radioactive iodine poses a particularly grave threat, as exposure to it can disrupt human metabolism, heightening the risk of thyroid cancer. The intricate task of efficiently eliminating radioactive iodine under the elevated temperatures characteristic of real spent fuel reprocessing procedures stands as a formidable hurdle within the nuclear industry.[1,2] This challenge has spurred a consensus among researchers on both domestic and international fronts, highlighting the pressing need for the development of innovative and effective solid sorption materials.[3,4] The objective is to leverage the host−guest interactions between sorbents and radioactive iodine to achieve the highly efficient removal of radioactive pollutants. Thanks to the flourishing development of micro/mesoporous materials, an increasing number of emerging porous materials such as activated carbon,[5] zeolites,[6,7] metal−organic frameworks,[8,9] covalent organic frameworks,[10−13] and porous organic polymers,[14,15] among others,[16−18] have found applications in iodine removal. These materials, characterized by their intrinsic porosity, large specific surface area, and light elements such as C, H, O, and N, typically exhibit outstanding iodine sorption capabilities in laboratory settings. However, a notable discrepancy arises in the operational temperatures of iodine sorption experiments using these materials, and the vast majority are typically set at around 75 °C, which significantly deviates from the actual operating conditions of 120−150 °C.[1,3,4,19] Furthermore, the driving forces for iodine removal in these materials often hinge on weak interactions, posing a risk of iodine desorption at elevated temperatures. Currently, there are very few materials capable of effectively removing radioactive iodine under such high-temperature conditions,[10,19,20] underscoring the need for further research and development in this critical area.

The development of metal-modified sorption materials is a viable solution, utilizing their chemical reactions with I_2 to generate corresponding metal iodides and achieve the removal of radioactive iodine.[21−23] Various metals, such as Ag,[24−27] Cu,[28,29] Sn,[16,30] and Bi,[31−33] and their oxides have been investigated for this purpose. Among them, silver-based

Received: January 9, 2024
Revised: April 3, 2024
Accepted: April 7, 2024
Published: April 16, 2024

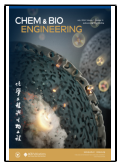

https://doi.org/10.1021/cbe.4c00010
Chem Bio Eng. 2024, 1, 548−558

Scheme 1. Preparation Steps for Bi@sSiO$_2$, Bi@HMS-1, and Bi@HMS-0[a]

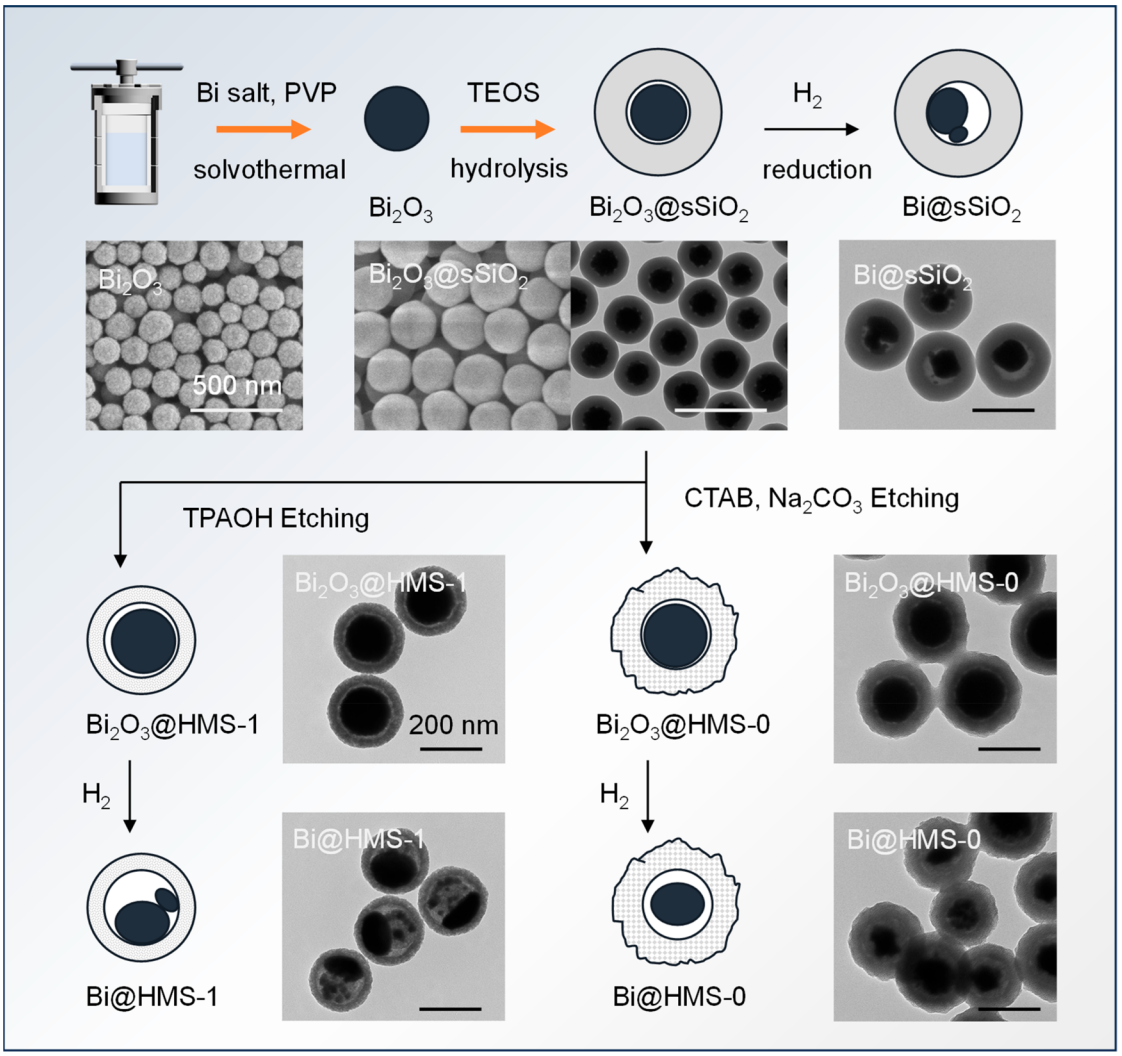

[a]The black and white scale bars represent 200 and 500 nm, respectively.

materials (SBMs) have undergone the most comprehensive fundamental research and are currently the most widely applied iodine sorption materials in the nuclear industry.[34,35] Relevant experimental results demonstrate that SBMs can selectively remove radioactive iodine under the high-temperature conditions typical of real-world operations, making them reliable iodine sorption materials in practical applications. However, due to silver being a precious metal, its expensive cost and relatively lower sorption capacity restrict further utilization in post-processing systems. To overcome these challenges, there is an imperative to develop other alternative low-cost yet effective metal elements that can match or exceed the performance of SBMs.

Since the groundbreaking work by Yang et al. from KAIST introducing the first bismuth-based materials (BBMs), which use a chemical reaction between Bi^0 and I_2 for the removal of radioactive iodine,[36,37] BBMs have become a focal point of research attention among researchers due to their relatively higher sorption capacity (typically 2−3 times that of SBMs) and cost-effectiveness.[31] Generally speaking, the sorption performance of BBMs for iodine is related to the following factors: the valence state of the bismuth component, particle size, and bismuth content, as well as the composition of the sorbent carrier, specific surface area, active site, and so on. Various types of bismuth-based composite materials have been developed to date, including carbon materials,[38−40] polymers,[23,41] layered double hydroxides (LDHs),[42] silica materials,[43,44] and so on. Materials based on carbon or polymers as frameworks often have higher sorption capacities, but most of them are attributed to the weak interaction between the carrier and iodine molecules. Inorganic-based materials, such as silica, show promise in reducing physisorbed iodine content when used as carriers due to their lower affinity with iodine. However, the synthesis of such composite materials often involves the H_2 reduction of bismuth components at high temperatures. Given the low melting point of metallic bismuth (271 °C), it tends to aggregate into large particles at elevated temperatures, leading to a significantly reduced utilization efficiency of bismuth and a notable decrease in iodine sorption capacity.[45] Furthermore, the lack of an apparent bonding interaction between bismuth components and carriers poses a risk of bismuth site detachment. In our previous work,[45] we found that when the content of bismuth in the sorbent reaches a certain level, due to the above reasons, it is difficult to continuously increase its iodine adsorption capacity by simply adding more bismuth content. Hence, the major challenge in

https://doi.org/10.1021/cbe.4c00010
Chem Bio Eng. 2024, 1, 548−558

this field is how to enhance iodine sorption capacity and maximize the proportion of chemical sorption capacity in the sorbents while preventing the detachment of bismuth components to ensure the stability of radioactive iodine on the sorbents.

Employing a strategy of confining bismuth components within the spatial constraints of silica-based materials to form a distinctive hollow structure resembling an egg might offer a viable solution. Similarly, Guan et al. reported a simple selective etching template method to construct hollow multi-shell materials with continuous interfaces, benefiting from the unique spatially separated environment where samples exhibit significantly enhanced catalytic activity.[55] In this work, based on a selective template etching strategy, we successfully obtained a monodisperse mesoporous silica-coated bismuth material (Bi@HMS-1) with a well-defined hollow core−shell structure by using SiO_2-coated Bi_2O_3 as a hard template and employing a gentle etching process involving an alkaline organic amine (tetrapropylammonium hydroxide, TPAOH). Subsequent electron microscopy images provided the most direct evidence that the hollow interior of Bi@HMS-1 not only ensures ample space for phase transitions during subsequent iodine capture processes, thereby preventing structural collapse, but also serves as a barrier, impeding the aggregation and detachment of bismuth components. Additionally, the absence of a pore templating agent results in shell channels with irregular distribution and lower pore volume in Bi@HMS-1. This characteristic proves advantageous in reducing the content of physisorbed iodine molecules, adding an extra layer of efficacy to the material. Under the synergistic effect of the above factors, the sorbent ultimately exhibits a superior decontamination effect on iodine.

EXPERIMENTAL SECTION

Materials. Bismuth nitrate pentahydrate ($Bi(NO_3)_3{\cdot}5H_2O$, AR), iodine (I_2, GR) and hexadecyltrimethylammonium bromide (CTAB, AR) were purchased from Shanghai Aladdin Biochemical Technology Co., Ltd. Urea (AR), polyvinylpyrrolidone (PVP, MW = 58 000), ethylene glycol (EG, AR), and tetraethyl orthosilicate (TEOS, AR) were purchased from Shanghai Macklin Biochemical Co., Ltd. Ethanol, nitric acid (HNO_3, AR), aqueous ammonia ($NH_3{\cdot}H_2O$, AR), sodium meta-aluminate ($NaAlO_2$, AR), and sodium carbonate (Na_2CO_3, AR) were purchased from Sinopharm Chemical Reagent Co., Ltd. Tetrapropylammonium hydroxide (TPAOH, 40 wt % in water) was purchased from Jiangsu Aikang Biopharmaceutical R&D Co., Ltd. Hydrogen (H_2, 99.999%) was purchased from Hangzhou Jingong Special Gas Co., Ltd. All reagents and materials are available on the market and were used without further purification.

Synthesis. Bi@HMS-1 and Bi@HMS-0 were synthesized through multiple steps, as shown in Scheme 1.

Synthesis of Bi_2O_3.[46] First, 0.485 g of $Bi(NO_3)_3{\cdot}H_2O$ was dissolved in 10 mL of HNO_3 (1 M) to obtain solution A. In a separate step, 0.4 g of urea and 0.45 g of PVP were dissolved in 50 mL of EG to obtain solution B. Solutions A and B were mixed together, and the resultant mixture was transferred to a reactor. Subsequently, a solvothermal reaction was conducted at 150 °C for 3 h. Following centrifugal washing and drying, the resulting Bi_2O_3 was obtained.

Synthesis of Bi_2O_3@sSiO$_2$. First, 0.8 g of Bi_2O_3 was added to 200 mL of ethanol and sonicated at 60 °C for 1 h. Subsequently, 4 mL of TEOS and a mixture comprising 6 mL of ammonia and 24 mL of DI water were added, and the solution was left to stir overnight. Following centrifugal washing and drying, Bi_2O_3@sSiO$_2$ was obtained.

Synthesis of Bi_2O_3@HMS-1. To begin, 1 g of Bi_2O_3@sSiO$_2$, 0.5165 mL of TPAOH, and 0.0835 mL of H_2O were put in a Teflon-lined and subject to ultrasound for 1 h. Then, the Teflon-lined was sealed in an autoclave and reacted at 140 °C for 1 h. After cooling to room temperature, the material was centrifuged, washed, and dried to obtain the material C. In the second stage, 0.15 g of C was mixed with 5 mL of 0.1 M TPAOH solution; then, 0.004 g of $NaAlO_2$ was added under agitation. After 30 min, the mixture was transferred to a Teflon-lined autoclave and reacted at 100 °C for 48 h. Finally, when it cooled to room temperature, centrifugal washing and drying were performed to obtain Bi_2O_3@HMS-1.

Synthesis of Bi@HMS-1. First, 1 g of Bi_2O_3@HMS-1 was placed in a tube furnace for H_2 reduction at a rate of 2 °C/min and heated to 400 °C for 4 h. Then, Bi@HMS-1 formed when it naturally cooled to room temperature.

Synthesis of Bi_2O_3@HMS-0.[49] First, 1.392 g of Bi_2O_3@SiO_2 was weighed based on 0.8 g of SiO_2 and poured into a round-bottomed flask. Then, 160 mL of water was added, and it was sonicated for 15 min. Next, 0.2 g of CTAB was added under agitation. After 30 min, 1.0176 g of Na_2CO_3 was added to the flask, which was then transferred to an oil bath pot and stirred at 95 °C for 4 h. At the end of the reaction, the solids were separated from the suspension by centrifugation and redispersed in 40 mL of water, which was then transferred to a Teflon-lined autoclave, where it reacted at 150 °C for 24 h. Finally, Bi_2O_3@HMS-0 was obtained after centrifugal washing and drying.

Synthesis of Bi@HMS-0. First, 1 g of Bi_2O_3@HMS-0 was placed in a tube furnace for H_2 reduction at a rate of 2 °C/min and heated to 300 °C for 4 h. Then, Bi@HMS-0 formed when it naturally cooled to room temperature.

Synthesis of HMS-1 or HMS-0. First, 0.1 g of Bi@HMS-1 or Bi@HMS-0 was mixed with 1 mL of concentrated nitric acid. Then, it was transferred into the Teflon-lined autoclave, reacting at 150 °C for 2 h. After cooling to room temperature, centrifugal washing and drying were performed to obtain bismuth-free samples.

Characterizations. Powder X-ray diffraction (PXRD) patterns of the samples were analyzed and determined with a PANalytical X'Pert Pro diffractometer in the 2θ range of 10−80°. The phases of samples were identified based on JCPDS standard cards. The textural properties of the samples were measured by N_2 physisorption at 77 K on an automatic specific surface and micropore analyzer (AUTOSORB-IQ2-MP), and the pore size distribution results were obtained by using the nonlocal density functional theory (NLDFT) model. Before the measurement, the samples were degassed under vacuum at 100 °C for 24 h. Fourier transform infrared (FTIR) spectra were obtained on a Thermo Scientific Nicolet iS10 spectrometer. Before the measurement, the samples were mixed with KBr and pressed into a wafer. The morphology and composition of the samples were characterized by scanning electron microscopy (SEM, SU8010). Transmission electron microscopy (TEM) and energy dispersive X-ray spectroscopy (EDX) images were obtained on Hitachi HT7700 and JEM-1230 instruments. X-ray photoelectron spectroscopy (XPS) spectra of the samples were measured on a Thermo Fisher ESCALAB Xi+ spectrometer. All peaks were corrected by setting the C 1s peak of 284.6 eV as the reference. Thermogravimetric (TG) curves of the samples were obtained on a TA-Q500 instrument at 600 °C under flowing air with a heating rate of 10 °C/min.

Iodine Sorption Experiments. The I_2 gas sorption experiments were conducted as follows. All experiments were repeated three times. Based on previous studies,[45] the volume of the sorption device and the mass of the added sorbents were 200 mL and 0.03 g, respectively. For static iodine sorption experiments at different temperatures (75, 130, and 200 °C), the relevant experimental conditions were as follows: the amount of iodine(s) added was 0.2 g, and the reaction time was fixed at 24 h. Subsequently, the total iodine sorbed capacity of the sorbents was calculated using eq 1, where q_e (mg/g) represents the iodine capture capacity of the sorbents and Δm (g) and m_s (g) are the mass change and initial mass of the sorbents, respectively.

$$q_e\ (\mathrm{mg/g}) = \Delta m/m_s \times 1000 \quad (1)$$

For the kinetic and thermodynamic sorption experiments of the sorbents, the reaction temperature was fixed at 130 °C. In the kinetic experiments, the amount of iodine(s) added to each sorption device

https://doi.org/10.1021/cbe.4c00010
Chem Bio Eng. 2024, 1, 548−558

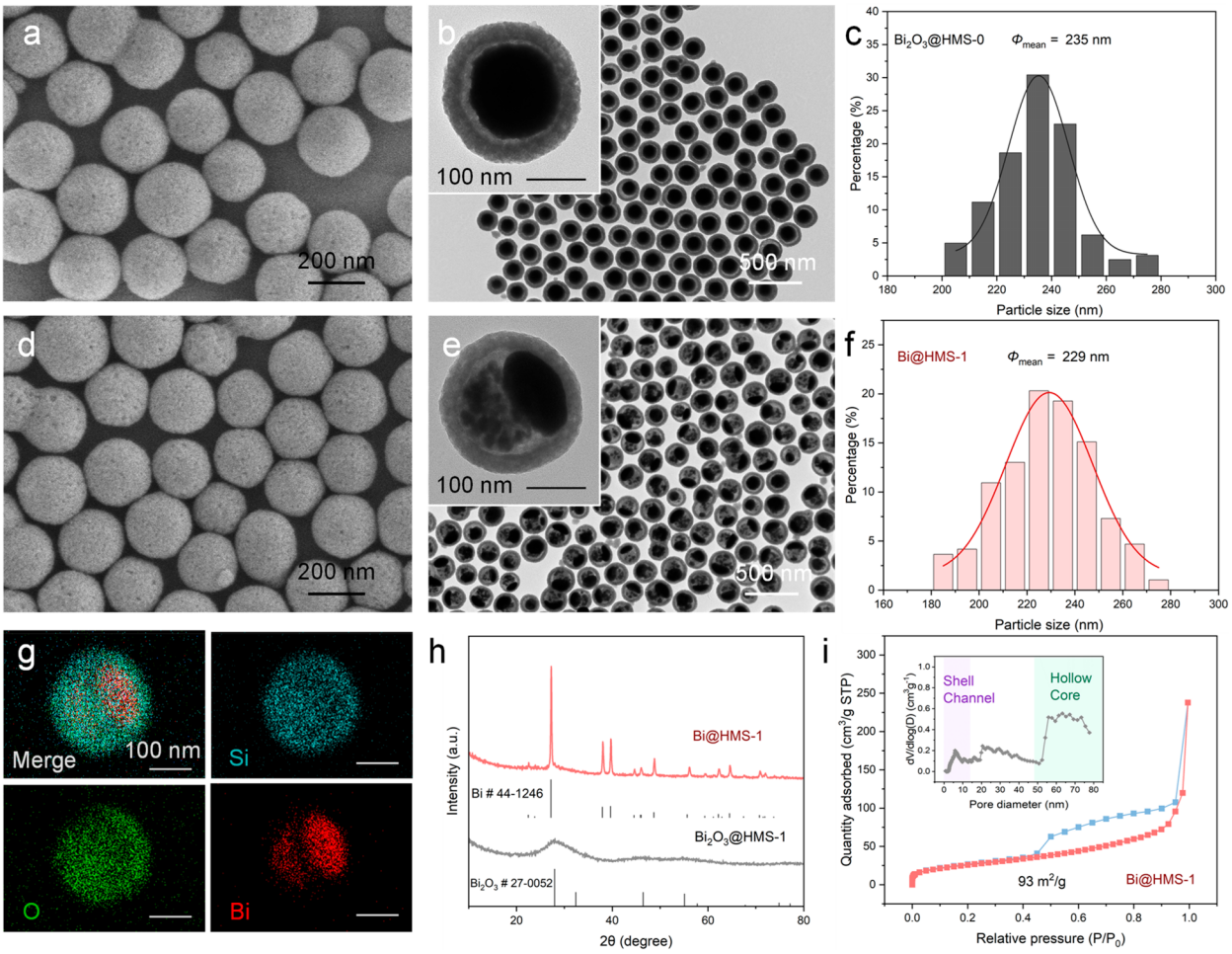

Figure 1. SEM, TEM, and particle size distribution images of (a, b, c) Bi_2O_3@HMS-1 and (d, e, f) Bi@HMS-1. (g) EDX mapping images of Bi@HMS-1. (h) PXRD patterns of Bi_2O_3@HMS-1 and Bi@HMS-1. (i) N_2 adsorption/desorption isotherms and pore size distribution of Bi@HMS-1.

was fixed at 0.2 g, and after different times (15, 30, 45, 60, 90, 120, 180, 300, and 480 min), one of the devices was removed, and its iodine sorption performance was evaluated by eq 1. In the thermodynamic experiment, based on the characteristics that solid iodine is easy to sublimate at high temperature, the experimental concentration was controlled by changing the amount of iodine(s) added in the sorption devices (0.010, 0.025, 0.040, 0.090, 0.140, 0.200, and 0.240 g). During the experiment, due to the weighing error, it was recorded and converted into the concentration according to the actual value. After 24 h of reaction, the iodine sorption performance of the samples was also evaluated by eq 1.

To gain a more comprehensive insight into the sorption behavior of the sorbents concerning iodine gas, desorption experiments were also conducted on the iodine-sorbed samples to evaluate the proportions of physisorbed or chemisorbed iodine. After iodine sorption, the samples were put into an iodine-free and unsealed device and kept at 130 °C for 4 h so that any physisorbed iodine could be desorbed. Then, the value of the chemisorbed iodine capacity could be obtained through eq 1, and the value of the physisorbed iodine capacity could be obtained by subtracting the chemisorbed iodine capacity from the value of the total sorbed iodine capacity.

Iodine Retention Experiments.[10] The iodine-loaded sorbents were placed in an empty open vial and then placed in an open wide-mouth bottle. The bottle containing the vial was kept at room temperature for different days. The vial containing the sample was weighed daily to calculate the change in its iodine sorption capacity.

RESULTS AND DISCUSSION

The morphological and structural characteristics of Bi@HMS-1 at various stages of the preparation process were first obtained through electron microscopy techniques. As shown in Figures S1 and S2, the diameter of the particles increased from the initial 148 to 276 nm after encapsulating Bi_2O_3 with a layer of SiO_2 by using the Stöber method.[46] Under the intense electron beam irradiation of TEM, a distinct solid core−shell structure was observed, with Bi_2O_3 confined to the core of the material (Bi_2O_3@sSiO_2). The N_2 adsorption/desorption curve of Bi_2O_3@sSiO_2 is shown in Figure S3, which belongs to a typical type III isotherm. Only when the pressure is further increased to the high-pressure region does the N_2 adsorption capacity increase significantly, indicating the non-porous property of the material with a small specific surface area of 10 m^2/g. Additionally, the pore size distribution result constructed by the NLDFT model also shows a negligible pore volume. Direct H_2 reduction of Bi_2O_3@sSiO_2 resulted in a silica-coated elemental bismuth material (Bi@sSiO_2), as confirmed by PXRD and TEM analyses of its phase structure composition (Figure S4). Unfortunately, at this stage, the shell was composed of dense SiO_2, hindering the mass transfer of iodine to the bismuth in the inner core due to the larger kinetic size of I_2 (0.335 nm) compared to that of H_2 (0.289 nm), resulting in the loss of iodine sorption capability. To overcome this hurdle, we introduced TPAOH, an alkaline organic amine

https://doi.org/10.1021/cbe.4c00010
Chem Bio Eng. 2024, 1, 548−558

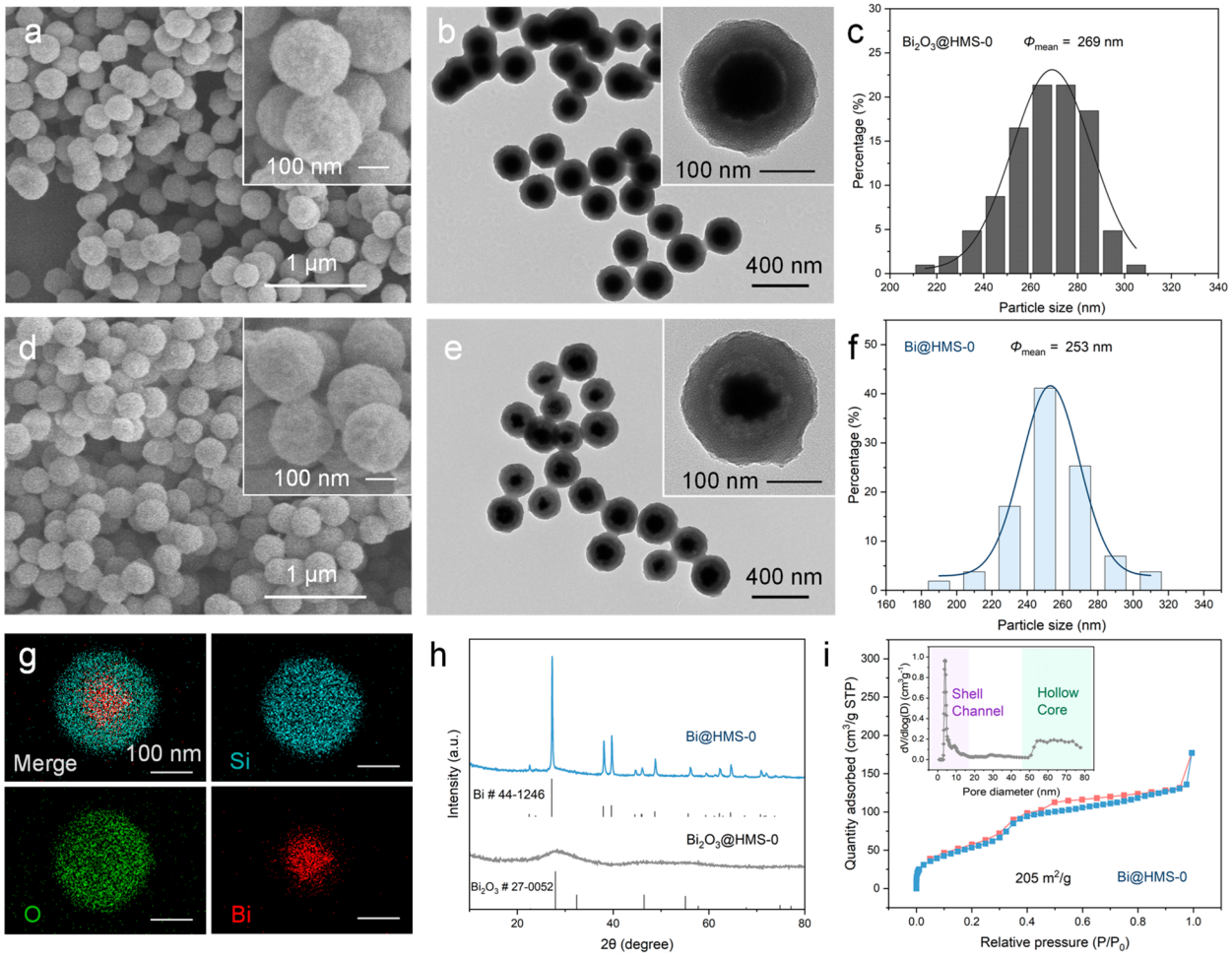

Figure 2. SEM, TEM, and particle size distribution images of (a, b, c) Bi_2O_3@HMS-0 and (d, e, f) Bi@HMS-0. (g) EDX mapping images of Bi@HMS-1. (h) PXRD patterns of Bi_2O_3@HMS-0 and Bi@HMS-0. (i) N_2 adsorption/desorption isotherms and pore size distribution of Bi@HMS-0.

etching agent, which is commonly used as a structure-directing agent in the preparation of microporous zeolites, as a pore-forming agent for the dense SiO_2 shell channels. Under alkaline conditions, hydroxyl groups on the SiO_2 surface undergo deprotonation, presenting a negatively charged surface. At this point, TPA^+ cations in the solution electrostatically bind to the surface, preventing SiO_2 from undergoing excessive etching dissolution under attack by OH^-, thus preserving the regular core−shell structure.[47] The morphology and structure of Bi_2O_3@HMS-1, as shown in Figure 1a−c, reveal that under TPAOH etching, the originally smooth surface becomes uneven. In the TEM images, it can be seen that the shell layer at this stage is composed of numerous nanoscale SiO_2 clusters, creating interstitial spaces that serve as diffusion channels for iodine molecules. The overall particle size is reduced from 276 nm of Bi_2O_3@sSiO_2 to 235 nm. Following high-temperature H_2 reduction treatment, the surface of Bi@HMS-1 exhibits no apparent changes, but the originally regular spherical structure inside becomes flattened, adhering to one side of the hollow shell layer like a droplet, with a corresponding average particle size of 112 nm (Figures 1d,e and S5). The SEM image of the sample with the crushed structure is shown in Figure S6, and a clear hollow structure resembling an egg shell can be observed. This is attributed to the low melting point of bismuth, and at the reduction temperature (400 °C), the reduced bismuth particles have already melted and closely adhered to one side of the spherical structure. The electron microscopy results again confirm the success of the confinement strategy, as the shell construction inhibits further fusion and aggregation of bismuth particles. Additionally, in the 500 nm scale image (Figure 1e), some particles retain a regular circular core, which can be explained by observing from different angles. Subsequently, EDX mapping of Bi@HMS-1 visually affirmed the impeccable encapsulation of Bi elements within Si and O elements. PXRD provided valuable insights into the phase structure, indicating that the initially poorly crystalline Bi_2O_3@HMS-1, following H_2 reduction, displayed remarkably sharp diffraction peaks, matching well with the PDF card of Bi^0.[45] By measuring the half-peak width of the (012) crystal face of Bi@HMS-1 and bringing it into Scherrer's formula, the average crystal size of Bi^0 can be obtained as 44 nm, indicating that the bismuth nanoparticles observed in the TEM image are not a perfect single crystal but are composed of many smaller crystals. To comprehensively assess its physical properties, N_2 adsorption/desorption tests were performed to obtain the surface area and pore structure information of Bi@HMS-1. As shown in Figure 1i, Bi@HMS-1 exhibited a typical type II isotherm with a surface area of 93 m^2/g. A significant H3-type hysteresis loop appears at medium to high pressures, reflecting its characteristic hollow structure.[47,48] By combining the TEM results, the pore size distribution result unveiled two distinct regions: the

https://doi.org/10.1021/cbe.4c00010
Chem Bio Eng. 2024, 1, 548−558

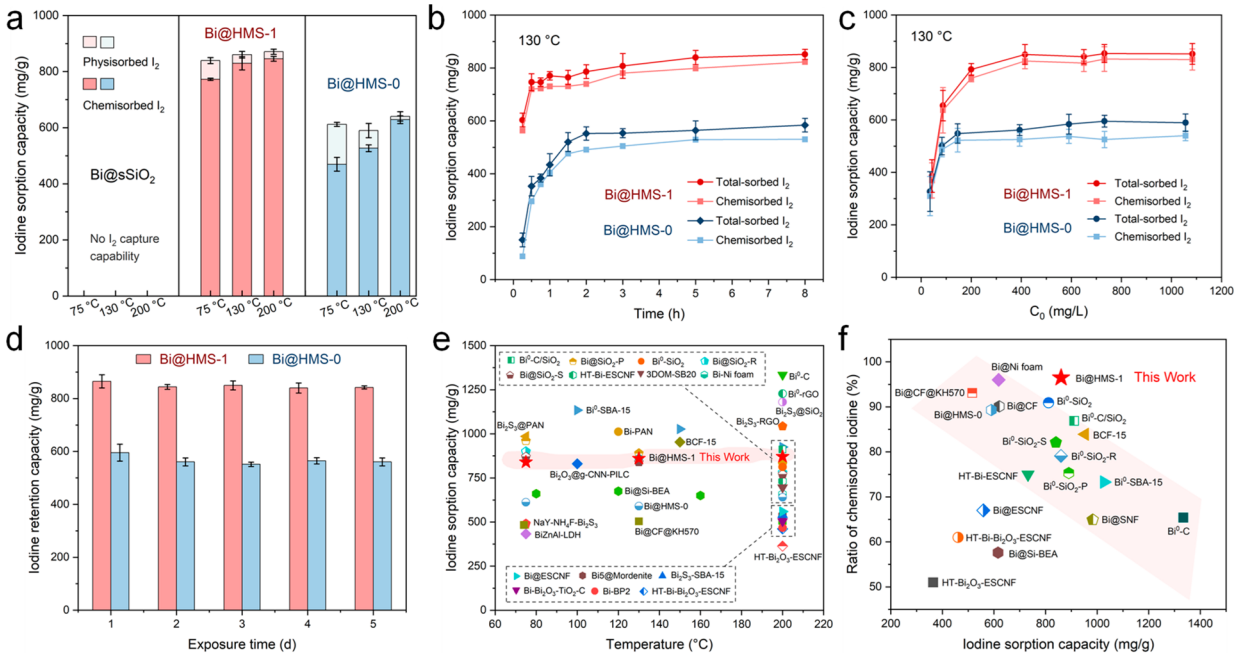

Figure 3. (a) Static I_2 sorption experiments of Bi@sSiO_2, Bi@HMS-1, and Bi@HMS-0 at different temperatures. The (b) kinetics and (c) isothermal sorption experiments of Bi@HMS-1 and Bi@HMS-0. (d) The I_2 retention capacity of I_2-Bi@HMS-1 and I_2-Bi@HMS-0 after different exposure days to room temperature and atmospheric pressure air. (e) Comparison of iodine sorption capacities of reported BBMs, Bi@HMS-1, and Bi@HMS-0 at different temperatures. (f) Comparison between the total iodine sorption capacity and chemisorption ratio of different BBMs, Bi@HMS-1 and Bi@HMS-0.

portion smaller than 10 nm corresponded to the mesoporous channels formed by TPAOH etching in the shell, while the portion larger than 50 nm matched the large hollow inner core of the material. Noteworthy is the absence of the addition of traditional organic template agents, and the shell of Bi@HMS-1 exhibited a relatively low pore volume and irregular pore size distribution. While this may be deemed unfavorable in scenarios necessitating a broad specific surface area for optimal active site distribution, it aligns precisely with our desired outcome in this case. The non-dense shell serves as channels for guest molecules' entry and exit transfer, and the low specific surface area and pore volume prove instrumental in significantly minimizing the physisorption of iodine.

On the other hand, by referring to the conventional inorganic base (Na_2CO_3) and organic template agent (CTAB) etching methods, we synthesized a mesoporous silica-coated bismuth material (Bi@HMS-0) with uniformly distributed mesoporous channels.[49] In comparison to Bi@HMS-1, Bi@HMS-0 exhibits a larger specific surface area and pore volume. It is essential to highlight that, due to the incorporation of the organic template agent, the dissolution and recondensation of silica species during the synthesis process inevitably led to bridging between the surfaces of numerous particles, preventing the achievement of perfect monodispersity. The corresponding morphology and structure of Bi@HMS-0 are shown in Figure 2, and it has an average particle size of 253 nm, a specific surface area of 205 m^2/g, and channels concentrated in the shell layer distributed at 3.9 nm. Finally, in order to more intuitively understand the differences between Bi@HMS-1 and Bi@HMS-0 in the shell pore structure, bismuth-free samples were obtained by selectively dissolving the bismuth component core of the materials with an acid solution and named HMS-1 and HMS-0, respectively. Their N_2 absorption/desorption curves and pore size distributions are shown in Figure S7, which shows a trend basically consistent with those of Bi@HMS-1 and Bi@HMS-0. However, due to the absence of the Bi core, the area of the hysteresis loop in the curves is obviously larger, and the pore size of the hollow part is also extended. The corresponding specific surface areas increased from 93 and 205 to 167 and 301 m^2/g, respectively.

In the evaluation tests of iodine sorption performance, we conducted relevant iodine sorption experiments at three representative temperatures within the iodine sorption field.[44,50,51] Subsequently, high-temperature desorption experiments were performed on the sorbed samples to obtain the distribution of physical/chemical sorbed iodine.[45] The results, as depicted in Figure 3a, showed that due to the dense shell of Bi@sSiO_2, no iodine sorption capability was observed. In contrast, both Bi@HMS-1 and Bi@HMS-0 exhibited good sorption capacities at 75, 130, and 200 °C, ranging between 820−870 and 590−620 mg/g, respectively. Notably, at 130 °C, Bi@HMS-1 demonstrated a superior iodine sorption capacity compared to Bi@HMS-0, with significantly lower content of physisorbed iodine, approaching negligible levels, perfectly achieving the original design of this work. The observed trend of decreasing physisorbed iodine with increasing temperature aligns with thermodynamic principles: generally, the capture and binding of guest molecules by solid-phase sorbents is an entropy decreasing process, mostly exothermic reactions, which are unfavorable at high temperatures. As the temperature increases, the sequential reduction in physisorption of iodine becomes evident.[1,3] Subsequently, we conducted dynamic and isothermal sorption experiments on Bi@HMS-1 and Bi@HMS-0 at 130 °C, which were close to those encountered in actual spent nuclear fuel reprocessing. Unexpectedly, in the kinetic data, Bi@HMS-1 not only demonstrated a superior iodine sorption capacity but also

https://doi.org/10.1021/cbe.4c00010
Chem Bio Eng. 2024, 1, 548−558

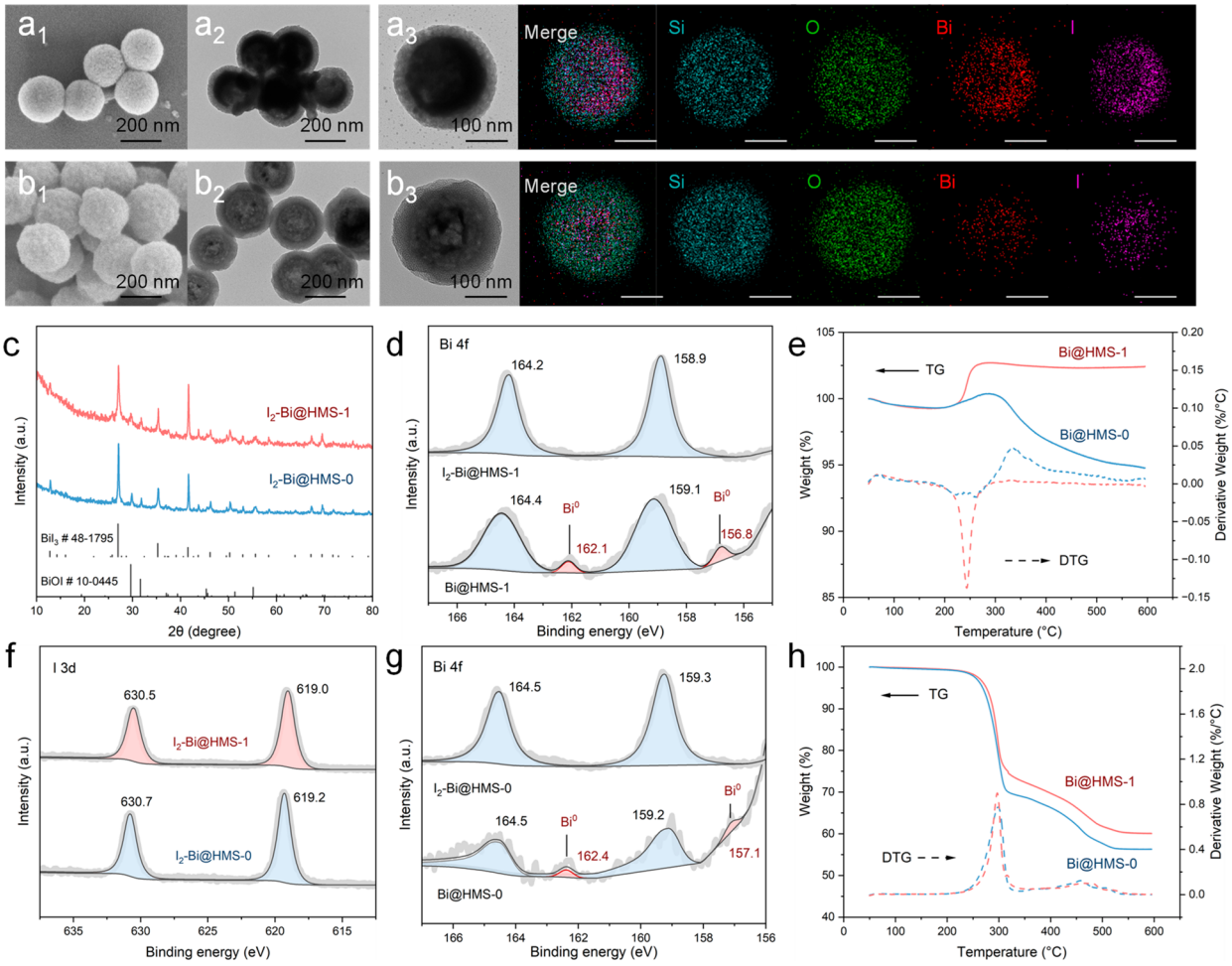

Figure 4. SEM, TEM, and EDX mapping images of (a_{1-3}) I_2-Bi@HMS-1 and (b_{1-3}) I_2-Bi@HMS-0. (c) PXRD patterns of I_2-Bi@HMS-1 and I_2-Bi@HMS-0. (d) Bi 4f XPS spectra of I_2-Bi@HMS-1 and Bi@HMS-1. TG and DTG curves of Bi@HMS-1 and Bi@HMS-0 (e) before or (h) after capturing iodine. (f) I 3d XPS spectra of I_2-Bi@HMS-1 and I_2-Bi@HMS-0. (g) Bi 4f XPS spectra of I_2-Bi@HMS-0 and Bi@HMS-0.

exhibited a faster equilibrium time compared to Bi@HMS-0. This phenomenon can be attributed to its thinner silica shell, which serves to reduce the diffusion time for iodine molecules entering the material. To comprehensively assess the removal capacity of the sorbents at different initial iodine concentrations, isothermal sorption experiments were conducted. The results indicate that at lower initial iodine concentrations, the sorbents primarily remove iodine through chemisorption. Bi@HMS-0 reaches sorption equilibrium at an I_2 concentration of ~200 mg/L with a saturated sorption capacity of approximately 550 mg/g. In contrast, Bi@HMS-1 reaches equilibrium at an I_2 concentration of ~400 mg/L with a saturated sorption capacity of about 850 mg/g. However, it must be noted that although the same raw material was used in the preparation process of Bi@HMS-1 and Bi@HMS-0 and Bi_2O_3@sSiO_2 was used as the template, the differences in subsequent experimental methods eventually led to obvious differences in the shell thickness of the obtained samples (36 and 54 nm, respectively). Therefore, in order to eliminate the effect of inconsistent shell thickness, a sample (Bi@HMS-0-2mL) with similar shell thickness (38 nm) to Bi@HMS-1 was obtained by reducing the amount of TEOS to 2 mL during the preparation of Bi_2O_3@sSiO_2-2mL (Figure S8). Iodine sorption experiments show that the saturated sorption capacity of Bi@HMS-0-2mL was 752 mg/g, and the chemisorption ratio was 92.3%, which is much higher than that of Bi@HMS-0 but still lower than that of Bi@HMS-1. These results further highlight the advantages of using TPAOH as an etching agent. Lastly, the stability of iodine on the sorbents was evaluated by directly exposing I_2-Bi@HMS-1 and I_2-Bi@HMS-0 (without desorption) to air at room temperature and atmospheric pressure. The results showed that, given that the iodine sorbed by the sorbents is predominantly attributed to chemisorption, there is almost no risk of desorption leakage. This finding holds significant implications for the practical application of the sorbents. As shown in Figure 3e,f, we conducted a comprehensive comparison between the sorbents prepared in this work and the BBMs reported in the literature, with specific data provided in Tables S1 and S2. Throughout the entire experimental temperature range, the iodine sorption capacity of Bi@HMS-1 remains highly competitive. While it may not exhibit the optimum performance, it consistently stands among the leading sorbents. On the other hand, when plotting the chemisorption ratio against the total iodine sorption capacity, Bi@HMS-1 not only secures a top position for total iodine sorption capacity but also achieves an impressive chemisorption ratio of 96.5%. To the best of our knowledge, this positions Bi@HMS-1 at the forefront among BBMs with relevant data, even surpassing the Bi@Ni foam sorbent

https://doi.org/10.1021/cbe.4c00010
Chem Bio Eng. 2024, 1, 548−558

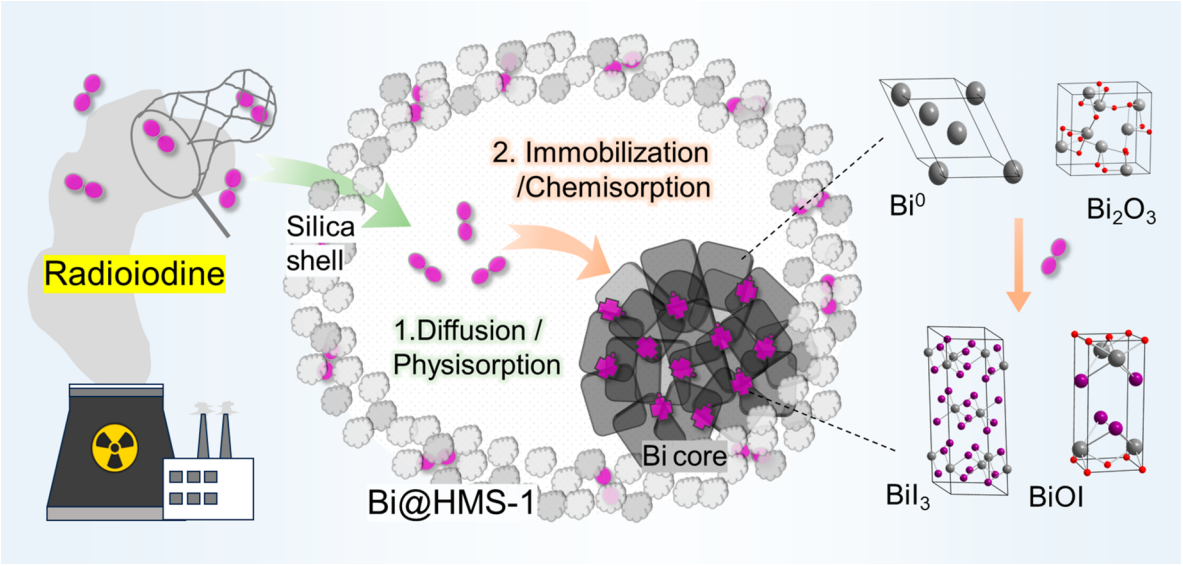

Figure 5. Schematic diagram of the removal process of I_2 by Bi@HMS-1.

prepared with a framework consisting entirely of non-micro/mesoporous structures.[52]

The remarkable sorption capacity of the sorbents for iodine encouraged us to further analyze the interactions between the sorbents and iodine molecules. As depicted in Figure 4, we initially investigated the morphological changes of Bi@HMS-1 and Bi@HMS-0 after capturing iodine by using electron microscopy techniques. In the case of I_2-Bi@HMS-1, the originally hollow interior underwent a substantial transformation, becoming densely packed with a dark substance that nearly entirely filled the core. Additionally, some of this dark substance penetrated the shell and extended to the exterior. Conversely, the core of I_2-Bi@HMS-0 became discrete, displaying numerous overlapping black sheet-like structures. Through EDX mapping and subsequent PXRD analysis, we successfully identified the aforementioned black substances as BiI_3 and BiOI. These compounds emerged as a result of the chemical reaction between the bismuth core and iodine molecules. The well-known sorption process involves reactions between Bi^0 and I_2 to form BiI_3. Regarding the generation of BiOI, insights were gleaned from the XPS results (Figures 4 and S9).[45] As shown in Figure 4d,g, in the Bi 4f spectra of Bi@HMS-1 and Bi@HMS-0, we observed that the Bi elements in the initial samples existed not only in the 0-valent state but also partially in the +3-oxidation state. Given that XPS is a surface analysis technique renowned for its detection precision within a few nanometers, Bi^{3+} is likely to be present as a thin layer of oxide film attached to the surface of Bi^0, similar to the alumina film on the surface of aluminum. Due to the minimal thickness of the oxide layer, no diffraction peaks of Bi_2O_3 were detected in the previous PXRD tests of Bi@HMS-1. After capturing iodine, only Bi^{3+} was detected. In the I 3d spectra, only one chemical environment of iodine was observed, matching the binding energy of the −1 state, with no appearance of peaks corresponding to 0-valent iodine, further confirming the minimal physisorption of iodine on the sorbent. Combined with the information from the literature,[45] it can be inferred that the diffraction peak of BiOI detected in the PXRD pattern of I_2-Bi@HMS-1/0 was the result of the chemical reaction between the Bi_2O_3 film on the surface of the Bi^0 and the iodine molecule. Due to the small content of Bi_2O_3, its diffraction peak intensity is much smaller than that of BiI_3. As for the observed differences in morphology following the reaction, we speculate correlation with the initial morphology of the bismuth core in the sorbents. In the preparation process of Bi@HMS-1, due to the necessity to entirely remove TPAOH, the H_2 reduction temperature reached 400 °C, far exceeding the melting point of Bi^0. Consequently, the resulting core adheres to one side of the sphere like a droplet. When it comes into contact with I_2 diffusing from the shell channel, the reaction products of bismuth iodide mainly grow towards the hollow side of the sphere, gradually filling the originally spacious core. Finally, the thermal stability of Bi@HMS-1 and Bi@HMS-0 before and after capturing iodine was evaluated through TGA−DTG (thermogravimetric analysis and derivative thermogravimetry) tests in an air atmosphere. The results, as shown in Figure 4e,h, indicate that the oxidation of Bi@HMS-1 and Bi@HMS-0 in air primarily occurs around 250 °C. The mass reduction of Bi@HMS-0 above 300 °C may be attributed to the decomposition of residual hydrocarbons. For the samples after capturing iodine, I_2-Bi@HMS-1 and I_2-Bi@HMS-0 exhibit similar thermal decomposition patterns, undergoing significant degradation (BiI_3) at 300 °C.[45] Since I_2-Bi@HMS-1 sorbed more iodine than I_2-Bi@HMS-0, the residual mass at the end of the curve is less.

Based on these results, a mechanism for iodine sorption by Bi@HMS-1 is proposed (Figure 5). In a nanoscale hollow core−shell reactor, iodine molecules first diffuse from the mesoporous channels of the shell to the bismuth core, where they subsequently undergo chemical reactions to form fixed bismuth iodide compounds. Due to the small pore volume of the channels, only a very small fraction of iodine is physisorbed on the shell. In the case of Bi@HMS-0, due to the larger pore volume of the shell channels, a higher H_2 reduction temperature (400 °C) will cause leakage of bismuth outside the shell (Figure S10). Accordingly, the temperature is set at 300 °C to circumvent this issue. Consequently, the Bi^0 generated in Bi@HMS-0 does not adhere closely to one side of the sphere, like in Bi@HMS-1, but rather concentrates towards the middle. Due to the lower reduction temperature, as indicated by the FTIR results in Figure S11, some residual hydrocarbons are still detectable in Bi@HMS-0.[53] Upon

https://doi.org/10.1021/cbe.4c00010
Chem Bio Eng. 2024, 1, 548−558

exposure to iodine molecules, the reaction with the bismuth core in Bi@HMS-0 extends outward along the surface of the core, resulting in the formation of these loosely intertwined black sheet-like substances.

CONCLUSION

In conclusion, we successfully obtained two bismuth-based mesoporous silica composite materials with typical hollow core−shell structures by using different types of etching agents. In contrast to the conventional approach involving inorganic alkali combined with organic template etching, the use of TPAOH as an etching agent allowed the synthesis of nearly perfectly monodisperse samples, with bismuth components resembling droplets adhering to one side of the sphere. Under the dual action of TPA^+ cation protection and OH^- etching, the resulting Bi@HMS-1 not only maintained the core−shell structure of the hard template (Bi_2O_3@sSiO_2) but also exhibited a larger internal space, a thinner and more disordered shell, and a smaller pore volume. Comprehensive sorption experiments, systematic characterizations, and data comparisons confirmed the crucial role of the mentioned parameters in enhancing the chemisorption capacity of the sorbent while reducing the content of physisorbed iodine. The hollow, disordered shell of Bi@HMS-1 not only effectively inhibits the migration and agglomeration of bismuth components during the high-temperature reduction process but also acts as a radioactive barrier to firmly fix the sorbed iodine molecules in the core of the sorbent. Under these multiple effects, Bi@HMS-1 achieves an ultrahigh iodine sorption capacity of 850 mg/g at conditions close to the actual operating temperature of the post-treatment system, with chemical sorption accounting for 96.5%, which is highly competitive among the relevant iodine sorption materials. Finally, beyond its significance in the realm of radioactive iodine removal, this work contributes valuable insights for the design and synthesis of new materials, energy storage, environmental catalysis, and other related areas.

ASSOCIATED CONTENT

Supporting Information

The Supporting Information is available free of charge at https://pubs.acs.org/doi/10.1021/cbe.4c00010.

Additional morphology and particle size distribution data, BET data, XPS spectra, FTIR results characterization, and iodine sorption properties comparison tables (PDF)

AUTHOR INFORMATION

Corresponding Author

Chengliang Xiao − *College of Chemical and Biological Engineering, Zhejiang University, Hangzhou 310058, P.R. China; Institute of Zhejiang University-Quzhou, Quzhou 324000, P.R. China;* orcid.org/0000-0001-5081-2398; Email: xiaoc@zju.edu.cn

Authors

Zhenjiang Tian − *College of Chemical and Biological Engineering, Zhejiang University, Hangzhou 310058, P.R. China*

Tien-Shee Chee − *Department of Materials Science and Engineering, Korea Advanced Institute of Science and Technology, Daejeon 34141, South Korea*

Yuxun Hao − *College of Chemical and Biological Engineering, Zhejiang University, Hangzhou 310058, P.R. China*

Kang Kang − *College of Chemical and Biological Engineering, Zhejiang University, Hangzhou 310058, P.R. China*

Xiaofan Yang − *College of Chemical and Biological Engineering, Zhejiang University, Hangzhou 310058, P.R. China;* orcid.org/0000-0002-4916-7050

Complete contact information is available at: https://pubs.acs.org/10.1021/cbe.4c00010

Notes

The authors declare no competing financial interest.

ACKNOWLEDGMENTS

This research was made possible as a result of a generous grant from the National Natural Science Foundation of China (U2067213 and 22176017). The authors also thank Mrs. Sudan Shen at State Key Laboratory of Chemical Engineering in Zhejiang University for the TEM tests.

REFERENCES

(1) Wang, J.; Fan, D.; Jiang, C.; Lu, L. Host-guest interaction-mediated nanointerface engineering for radioiodine capture. *Nano Today* **2021**, *36*, 101034−101055.

(2) Huve, J.; Ryzhikov, A.; Nouali, H.; Lalia, V.; Augé, G.; Daou, T. Porous sorbents for the capture of radioactive iodine compounds: a review. *RSC Adv.* **2018**, *8*, 29248−29273.

(3) Pan, T.; Yang, K.; Dong, X.; Han, Y. Adsorption-based Capture of Iodine and Organic Iodides: Status and Challenges. *J. Mater. Chem. A* **2023**, *11*, 5460−5475.

(4) Riley, B. J.; Carlson, K. Radioiodine sorbent selection criteria. *Front. Chem.* **2022**, *10*, 969303−969311.

(5) Yang, X.; Xie, D.; Wang, W.; Li, S.; Tang, Z.; Dai, S. An activated carbon from walnut shell for dynamic capture of high concentration gaseous iodine. *Chem. Eng. J.* **2023**, *454*, 140365.

(6) Pan, T.; Dong, X.; Han, Y. Efficient capture of iodine and methyl iodide using all-silica EMM-17 zeolite. *Nano Res.* **2023**, *16*, 6308−6315.

(7) Pham, T. C. T.; Docao, S.; Hwang, I. C.; Song, M. K.; Choi, D. Y.; Moon, D.; Oleynikov, P.; Yoon, K. B. Capture of iodine and organic iodides using silica zeolites and the semiconductor behaviour of iodine in a silica zeolite. *Energy Environ. Sci.* **2016**, *9*, 1050.

(8) Chen, P.; He, X.; Pang, M.; Dong, X.; Zhao, S.; Zhang, W. Iodine Capture Using Zr-Based Metal-Organic Frameworks (Zr-MOFs): Adsorption Performance and Mechanism. *ACS Appl. Mater. Interfaces* **2020**, *12*, 20429−20439.

(9) Ju, Y.; Li, Z.; Qiu, J.; Li, X.; Yang, J.; Zhang, Z.; He, M.; Wang, J.; Lin, J. Adsorption and Detection of Iodine Species by a Thorium-Based Metal-Organic Framework. *Inorg. Chem.* **2023**, *62*, 8158−8165.

(10) He, L.; Chen, L.; Dong, X.; Zhang, S.; Zhang, M.; Dai, X.; Liu, X.; Lin, P.; Li, K.; Chen, C.; Pan, T.; Ma, F.; Chen, J.; Yuan, M.; Zhang, Y.; Chen, L.; Zhou, R.; Han, Y.; Chai, Z.; Wang, S. A nitrogen-rich covalent organic framework for simultaneous dynamic capture of iodine and methyl iodide. *Chem.* **2021**, *7*, 699−714.

(11) Cheng, K.; Li, H.; Li, Z.; Li, P.; Zhao, Y. Linking Nitrogen-Rich Organic Cages into Isoreticular Covalent Organic Frameworks for Enhancing Iodine Adsorption Capability. *ACS Mater. Lett.* **2023**, *5*, 1546−1555.

(12) Liu, X.; Zhang, A.; Ma, R.; Wu, B.; Wen, T.; Ai, Y.; Sun, M.; Jin, J.; Wang, S.; Wang, X. Experimental and theoretical insights into copper phthalocyanine-based covalent organic frameworks for highly efficient radioactive iodine capture. *Chin. Chem. Lett.* **2022**, *33*, 3549−3555.

(13) Jiang, B.; Qi, Y.; Li, X.; Guo, X.; Jia, Z.; Zhang, J.; Li, Y.; Ma, L. Efficient gaseous iodine capture enhanced by charge-induced effect of

covalent organic frameworks with dense tertiary-amine nodes. *Chin. Chem. Lett.* **2022**, *33*, 3556−3560.
(14) Zhang, H.; Gong, L.; Yin, M.; Xiong, X.; Zhang, Q.; Feng, X.; Luo, F.; Carney, J. B.; Yue, Y. Efficient organic iodide capture by a mesoporous bimetallic-organic framework. *Cell Rep. Phys. Sci.* **2022**, *3*, 100830−100842.
(15) Gao, X.; Hu, Q.; Shi, Y.; Liang, R.; Qiu, J. Rationally designing imidazole-based coordination polymers with high adsorption capacity for removing iodine. *Chem. Eng. J.* **2023**, *468*, 143838−143845.
(16) Zhang, Y.; He, L.; Pan, T.; Xie, J.; Wu, F.; Dong, X.; Wang, X.; Chen, L.; Gong, S.; Liu, W.; Kang, L.; Chen, J.; Chen, L.; Chen, L.; Han, Y.; Wang, S. Superior Iodine Uptake Capacity Enabled by an Open Metal-Sulfide Framework Composed of Three Types of Active Sites. *CCS Chemistry* **2023**, *5*, 1540−1548.
(17) Akram, B.; Lu, Q.; Wang, X. Polyoxometalate-Zirconia Coassembled Microdumbbells for Efficient Capture of Iodine. *ACS Mater. Lett.* **2020**, *2*, 461−465.
(18) Wan, H.; Xu, Q.; Wu, J.; Lian, C.; Liu, H.; Zhang, B.; He, J.; Chen, D.; Lu, J. SuFEx-Enabled Elastic Polysulfates for Efficient Removal of Radioactive Iodomethane and Polar Aprotic Organics through Weak Intermolecular Forces. *Angew. Chem. Int. Ed.* **2022**, *61*, e202208577.
(19) Zhang, Z.; Dong, X.; Yin, J.; Li, Z.; Li, X.; Zhang, D.; Pan, T.; Lei, Q.; Liu, X.; Xie, Y.; Shui, F.; Li, J.; Yi, M.; Yuan, J.; You, Z.; Zhang, L.; Chang, J.; Zhang, H.; Li, W.; Fang, Q.; Li, B.; Bu, X.; Han, Y. Chemically Stable Guanidinium Covalent Organic Framework for the Efficient Capture of Low-Concentration Iodine at High Temperatures. *J. Am. Chem. Soc.* **2022**, *144*, 6821−6829.
(20) Xu, M.; Wang, T.; Zhou, L.; Hua, D. Fluorescent conjugated mesoporous polymers with N,N-diethylpropylamine for the efficient capture and real time detection of volatile iodine. *J. Mater. Chem. A* **2020**, *8*, 1966−1974.
(21) Muhire, C.; Tesfay Reda, A.; Zhang, D.; Xu, X.; Cui, C. An overview on metal Oxide-based materials for iodine capture and storage. *Chem. Eng. J.* **2022**, *431*, 133816−133832.
(22) Moore, R.; Pearce, C.; Morad, J.; Chatterjee, S.; Levitskaia, T.; Asmussen, R.; Lawter, A.; Neeway, J.; Qafoku, N.; Rigali, M.; Saslow, S.; Szecsody, J.; Thallapally, P.; Wang, G.; Freedman, V. Iodine immobilization by materials through sorption and redox-driven processes: A literature review. *Sci. Total Environ.* **2020**, *716*, 132820−132830.
(23) Chong, S.; Riley, B. J.; Asmussen, R. M.; Fujii Yamagata, A. L.; Marcial, J.; Lee, S.; Burns, C. A. Iodine Capture with Metal-Functionalized Polyacrylonitrile Composite Beads Containing Ag^0, Bi^0, Cu^0, or Sn^0 Particles. *ACS Appl. Polym. Mater.* **2022**, *4*, 9040−9051.
(24) Zhang, J.; Pu, N.; Li, M.; Sang, W.; He, Q.; Tian, Q.; Zhang, W. High-efficient Ag(I) ion binding, Ag(0) nanoparticle loading, and iodine trapping in ultrastable benzimidazole-linked polymers. *Sep. Purif. Technol.* **2024**, *328*, 125052.
(25) Yadav, A.; Chong, S.; Riley, B.; McCloy, J.; Goel, A. Iodine Capture by Ag-Loaded Solid Sorbents Followed by Ag Recycling and Iodine Immobilization: An End-to-End Process. *Ind. Eng. Chem. Res.* **2023**, *62*, 3635−3646.
(26) Chebbi, M.; Azambre, B.; Monsanglant-Louvet, C.; Marcillaud, B.; Roynette, A.; Cantrel, L. Effects of water vapour and temperature on the retention of radiotoxic CH3I by silver faujasite zeolites. *J. Hazard. Mater.* **2021**, *409*, 124947.
(27) Choi, S.; Nan, Y.; Tavlarides, L. L. Kinetics of aging process on reduced Ag exchanged mordenite in dry air and humid air. *AIChE J.* **2021**, *67*, e17182.
(28) He, X.; Chen, L.; Xiao, X.; Gan, Y.; Yu, J.; Luo, J.; Dan, H.; Wang, Y.; Ding, Y.; Duan, T. Improved utilization of Cu0 for efficient adsorption of iodine in gas and solution by mesoporous Cu^0-SBA-15 via solvothermal reduction method. *Chem. Eng. J.* **2023**, *462*, 142175.
(29) Zhou, J.; Chen, Q.; Li, T.; Lan, T.; Bai, P.; Liu, F.; Yuan, Z.; Zheng, W.; Yan, W.; Yan, T. Porous Copper-Loaded Zeolites for High-Efficiency Capture of Iodine from Spent Fuel Reprocessing Off-Gas. *Inorg. Chem.* **2022**, *61*, 7746−7753.
(30) Wang, C.; Yao, H.; Cai, Z.; Han, S.; Shi, K.; Wu, Z.; Ma, S. $[Sn_2S_6]^{4-}$ Anion-Intercalated Layered Double Hydroxides for Highly Efficient Capture of Iodine. *ACS Appl. Mater. Interfaces* **2023**, *15*, 52496−52505.
(31) Hao, Y.; Tian, Z.; Liu, C.; Xiao, C. Recent advances in the removal of radioactive iodine by bismuth-based materials. *Front. Chem.* **2023**, *11*, 1122484.
(32) Levitskaia, T.; Qafoku, N.; Bowden, M.; Asmussen, R.; Buck, E.; Freedman, V.; Pearce, C. A Review of Bismuth(III)-Based Materials for Remediation of Contaminated Sites. *ACS Earth Space Chem.* **2022**, *6*, 883−908.
(33) Tesfay Reda, A.; Pan, M.; Zhang, D.; Xu, X. Bismuth-based materials for iodine capture and storage: A review. *J. Environ. Chem. Eng.* **2021**, *9*, 105279.
(34) Nenoff, T.; Rodriguez, M.; Soelberg, N.; Chapman, K. Silver-mordenite for radiologic gas capture from complex streams: Dual catalytic CH_3I decomposition and I confinement. *Microporous Mesoporous Mater.* **2014**, *200*, 297−303.
(35) Chibani, S.; Chebbi, M.; Lebègue, S.; Cantrel, L.; Badawi, M. Impact of the Si/Al ratio on the selective capture of iodine compounds in silver-mordenite: a periodic DFT study. *Phys. Chem. Chem. Phys.* **2016**, *18*, 25574−25581.
(36) Yang, J.; Shin, J.; Park, J.; Park, G.; Yim, M. Novel synthesis of bismuth-based adsorbents for the removal of ^{129}I in off-gas. *J. Nucl. Mater.* **2015**, *457*, 1−8.
(37) Yang, J.; Cho, Y.; Shin, J.; Yim, M. Bismuth-embedded SBA-15 mesoporous silica for radioactive iodine capture and stable storage. *J. Nucl. Mater.* **2015**, *465*, 556−564.
(38) Na, T.; Zhu, H.; Chen, P.; Liu, F.; Yi, Y.; Zhou, J.; Duan, T.; Lei, J. In-situ growth nanoscale zero-valent bismuth 3D honeycomb-like material for highly efficient selective capture of iodine vapor in complex environments. *Sep. Purif. Technol.* **2024**, *330*, 125421−125432.
(39) Chee, T.; Lee, S.; Ng, W. J.; Akmal, M.; Ryu, H. J. Bi^0-Reduced Graphene Oxide Composites for the Enhanced Capture and Cold Immobilization of Off-Gas Radioactive Iodine. *ACS Appl. Mater. Interfaces* **2023**, *15*, 40438−40450.
(40) Liu, S.; Zeng, Y.; Liu, J.; Li, J.; Peng, H.; Xie, H.; Zou, H.; Xiao, C.; Hua, X.; Bao, J.; Xian, L.; Li, Y.; Chi, F. Efficient capture and stable storage of radioactive iodine by bismuth-based ZIF-8 derived carbon materials as adsorbents. *Sep. Purif. Technol.* **2022**, *302*, 122151−122161.
(41) Yu, Q.; Jiang, X.; Cheng, Z.; Liao, Y.; Pu, Q.; Duan, M. Millimeter-sized Bi_2S_3@polyacrylonitrile hybrid beads for highly efficient iodine capture. *New J. Chem.* **2020**, *44*, 16759−16768.
(42) Dinh, T. D.; Zhang, D.; Tuan, V. N. High iodine adsorption performances under off-gas conditions by bismuth-modified ZnAl-LDH layered double hydroxide. *RSC Adv.* **2020**, *10*, 14360.
(43) Baskaran, K.; Elliott, C.; Ali, M.; Moon, J.; Beland, J.; Cohrs, D.; Chong, S.; Riley, B.; Chidambaram, D.; Carlson, K. Effects of NO_2 aging on bismuth nanoparticles and bismuth-loaded silica xerogels for iodine capture. *J. Hazard. Mater.* **2023**, *446*, 130644−130658.
(44) Wang, E.; Chen, L.; He, X.; Xiang, Y.; Jia, S.; Chen, Y.; Guo, Z.; Luo, J.; Dan, H.; Ding, Y.; Duan, T. Capture of iodine gas by Bi-based composites derived from rice husk: Influence of the type of support on the iodine adsorption and retention. *Chem. Eng. J.* **2023**, *465*, 143069−143068.
(45) Tian, Z.; Chee, T.; Meng, R.; Hao, Y.; Zhou, X.; Ma, B.; Zhu, L.; Duan, T.; Xiao, C. Incipient wetness impregnation to prepare bismuth-modified all-silica beta zeolite for efficient radioactive iodine capture. *Environmental Functional Materials* **2022**, *1*, 92−104.
(46) Qin, F.; Zhao, H.; Li, G.; Yang, H.; Li, J.; Wang, R.; Liu, Y.; Hu, J.; Sun, H.; Chen, R. Size-tunable fabrication of multifunctional Bi_2O_3 porous nanospheres for photocatalysis, bacteria inactivation and template-synthesis. *Nanoscale* **2014**, *6*, 5402−5409.
(47) Dai, C.; Zhang, A.; Liu, M.; Guo, X.; Song, C. Hollow ZSM-5 with Silicon-Rich Surface, Double Shells, and Functionalized Interior with Metallic Nanoparticles and Carbon Nanotubes. *Adv. Funct. Mater.* **2015**, *25*, 7479−7487.

https://doi.org/10.1021/cbe.4c00010
Chem Bio Eng. 2024, 1, 548−558

(48) Jiao, Y.; Forster, L.; Xu, S.; Chen, H.; Han, J.; Liu, X.; Zhou, Y.; Liu, J.; Zhang, J.; Yu, J.; D'Agostino, C.; Fan, X. Creation of Al-Enriched Mesoporous ZSM-5 Nanoboxes with High Catalytic Activity: Converting Tetrahedral Extra-Framework Al into Framework Sites by Post Treatment. *Angew. Chem. Int. Ed.* **2020**, *132*, 19646−19654.
(49) Fang, X.; Chen, C.; Liu, Z.; Liu, P.; Zheng, N. A cationic surfactant assisted selective etching strategy to hollow mesoporous silica spheres. *Nanoscale* **2011**, *3*, 1632−1639.
(50) Xie, Y.; Pan, T.; Lei, Q.; Chen, C.; Dong, X.; Yuan, Y.; Maksoud, W.; Zhao, L.; Cavallo, L.; Pinnau, I.; Han, Y. Efficient and simultaneous capture of iodine and methyl iodide achieved by a covalent organic framework. *Nat. Commun.* **2022**, *13*, 2878.
(51) Chee, T.; Tian, Z.; Zhang, X.; Lei, L.; Xiao, C. Efficient capture of radioactive iodine by a new bismuth-decorated electrospinning carbon nanofiber. *J. Nucl. Mater.* **2020**, *542*, 152526−152533.
(52) Tian, Z.; Chee, T.; Zhu, L.; Duan, T.; Zhang, X.; Lei, L.; Xiao, C. Comprehensive comparison of bismuth and silver functionalized nickel foam composites in capturing radioactive gaseous iodine. *J. Hazard. Mater.* **2021**, *417*, 125978−125987.
(53) Jin, Z.; Wang, L.; Zuidema, E.; Mondal, K.; Zhang, M.; Zhang, J.; Wang, C.; Meng, X.; Yang, H.; Mesters, C.; Xiao, F. Hydrophobic zeolite modification for in situ peroxide formation in methane oxidation to methanol. *Science* **2020**, *367*, 193−197.
(54) Liu, C.; Lan, J.; Yan, Q.; Wang, Z.; Xu, C.; Shi, W.; Xiao, C. Temperature-responsive alkaline aqueous biphasic system for radioactive wastewater treatment. *Chinese. Chem. Lett.* **2022**, *33*, 3561−3564.
(55) Xu, H.; Han, J.; Zhao, B.; Sun, R.; Zhong, G.; Chen, G.; Yamauchi, Y.; Guan, B. A facile dual-template-directed successive assembly approach to hollow multi-shell mesoporous metal-organic framework particles. *Nat. Commun.* **2023**, *14*, 8062.

https://doi.org/10.1021/cbe.4c00010
Chem Bio Eng. 2024, 1, 548−558